# Supporting Information

## Governing Equations

We model the full-cell device with the following governing equations that solve for $\Phi_1$ and $\Phi_2$[1]:

$$-\nabla \cdot (\sigma \nabla \Phi_1) = -aC_d \frac{\partial(\Phi_1 - \Phi_2)}{\partial t} \quad in\ \Omega,$$

$$-\nabla \cdot (\kappa \nabla \Phi_2) = aC_d \frac{\partial(\Phi_1 - \Phi_2)}{\partial t} \quad in\ \Omega,$$

where $\Phi_1$ is the electrical potential, $\Phi_2$ is the ionic potential, and $\Omega$ denotes the volume of the modeled device. Additionally, $a$ is the specific surface area, $\sigma$ is the electrical conductivity, $\kappa$ is the ionic conductivity, and $C_d$ is the intrinsic specific capacitance of the electrochemically active material. The experimental measurements of these parameters are used in the simulation. The anode current collector is grounded ($\Phi_1 = 0$ on $\Gamma_a$) and we apply a linearly increasing voltage on the cathode current collector ($\Phi_1 = \zeta t$ on $\Gamma_c$) to imitate the charging phase of the cyclic voltammetry (CV) experiment, where $\zeta$ is the scan rate. The rest of the device boundary is electrically insulated. We set the initial condition as $\Phi_1(x,t=0) = 0$ and $\Phi_2(x,t=0) = 0$ with $t \in (0,T_f]$, where $T_f$ is the final simulation time. We assume a constant salt concentration due to its 0.5% maximum change observed in preliminary simulations including concentration gradients. For materials with larger specific capacitance and surface area, e.g. the holey graphene framework benchmark material[2], explicit modeling of the mass transport effects with the conservation equation of salt concentration was introduced in our previous work[3].

## Optimization Setup

In our topology optimization problem, we consider a continuous volume fraction field $\rho$, namely density, as the design variable that determines the material composition at each location, e.g. $\rho(x) = 1$ indicates electrolyte-filled porous electrode and $\rho(x) = 0$ indicates pure electrolyte, as illustrated in Figure S6. We aim to maximize the capacitive energy storage subject to a minimum energy efficiency constraint formulated as

$$\max_{\rho \in [0,1]} \theta_0 = \frac{1}{2}(E_{cap} + E_{in} - E_{ohm}) \; subject\ to\ \theta_1 = \frac{E_{cap}}{E_{in}} \geq \eta_{min},$$

where $E_{in}$ is the input energy, $E_{cap}$ is the stored capacitive energy, and $E_{ohm}$ are ohmic losses due to Joule heating, with $E_{in} = E_{cap} + E_{ohm}$ and

$$E_{in} = \int_0^{T_f} \int_{\Gamma_c} \sigma \nabla \Phi_1 \cdot n \Phi_1 ds dt,$$

$$E_{cap} = \int_0^{T_f} \int_{\Omega} aC_d \frac{\partial(\Phi_1 - \Phi_2)}{\partial t}(\Phi_1 - \Phi_2) dv dt,$$

$$E_{ohm} = \int_0^{T_f} \int_{\Omega} (\sigma \nabla \Phi_1 \cdot \nabla \Phi_1 + \kappa \nabla \Phi_2 \cdot \nabla \Phi_2) dv dt.$$

This objective function is equivalent to energy storage in the absence of parameter penalization to be introduced in the next section.

The discrete adjoint problem is solved to compute the sensitivity of the QoI with respect to the design variable $\rho$. The sensitivity is then utilized to guide the design update in each iteration. The topology optimization framework and the full-cell simulation model are implemented with the finite element library Firedrake[4] which leverages the discrete adjoint capability from pyadjoint[5]. The design iterations use a Python implementation of the MMA algorithm[6,7].

**Filtering and Thresholding**

Topology optimization problems are often ill-posed, which commonly results in designs with highly oscillatory material distributions that resemble a checkerboard. To prevent such appearances, we apply the diffusion-reaction PDE filter introduced by Lazarov and Sigmund[8] by solving

$$-r^2\nabla^2\tilde{\rho} + \tilde{\rho} = \rho \quad in\ \Omega,$$

$$r^2\nabla\tilde{\rho}\cdot n = 0 \quad on\ \partial\Omega,$$

where $r$ is the filter radius. Solving this system imposes a minimum feature length scale on the resulting filtered density field $\tilde{\rho}$. As a result, high frequency oscillations in $\rho$ are mollified in $\tilde{\rho}$. However, as a setback, the filtered density field $\tilde{\rho}$ contains large transitional regions with intermediate material compositions, e.g. $\tilde{\rho}(x) = 0.5$, which is unphysical and unmanufacturable. Therefore, we apply a differentiable Heaviside projection

$$\bar{\rho} = \frac{\tanh 2 + \tanh\left(4(\tilde{\rho} - 0.5)\right)}{2\tanh 2}$$

to promote binary designs. The different density fields are illustrated in Figure S7.

**Parameter Penalization**

The model parameters are affected by the local material composition. Namely, the effective specific surface area, electric conductivity, and ionic conductivity are interpolated by

$$a = a_1\bar{\rho}^q,$$

$$\sigma = \sigma_1\bar{\rho}^p,$$

$$\kappa = \kappa_0 + (\kappa_1 - \kappa_0)\bar{\rho}^p,$$

where $a_1$ and $\sigma_1$ are specific surface area and electric conductivity of the porous electrode material, and $\kappa_0$ is the pure electrolyte conductivity. $\kappa_1$ is the ionic conductivity through the electrode

material influenced by its pore network tortuosity and is computed via the modified Bruggeman correlation introduced by Madabattula and Kumar[9]

$\kappa_1 = f_m \epsilon^{1.5} \kappa_0$,

where $\epsilon$ is the porosity of the electrode material and $f_m = 0.1$ is a correction coefficient. Values for $a_1$, $\sigma_1$, $\kappa_0$, and $\epsilon$ are obtained via experimental measurements. $p$ and $q$ are a user-defined exponents that takes different sets of values in the forward simulation and QoI computation, to penalize intermediate materials by making their performance unfavorable, thus promoting a binary optimized design. We choose $p = 1.5,\ q = 1.0$ in the forward simulation and $p = 1.0,\ q = 3.0$ in the QoI computations. This different interpolation is illustrated in Figure S8.

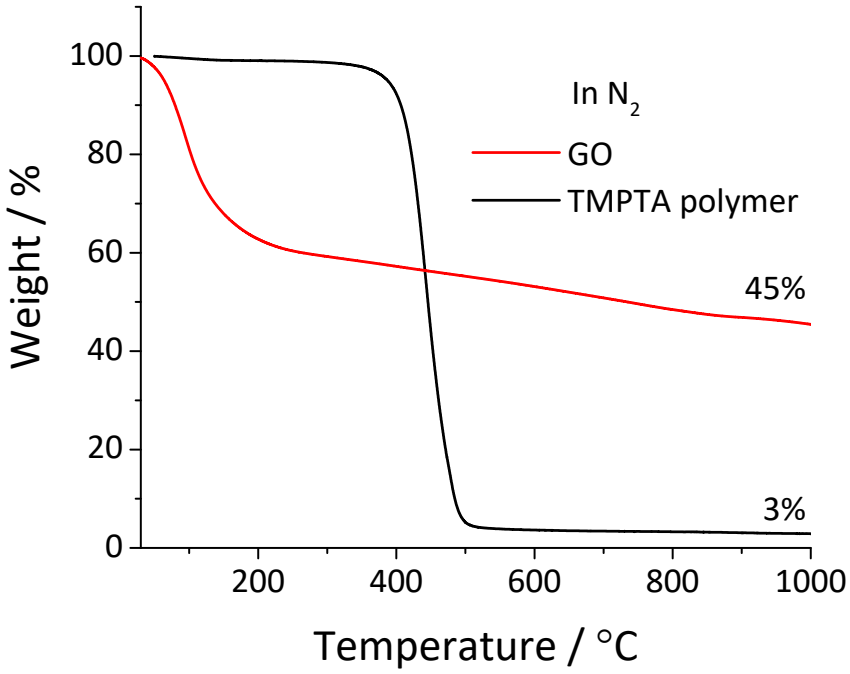


Figure S1. TGA curves of TMPTA polymer and GO in $N_2$.

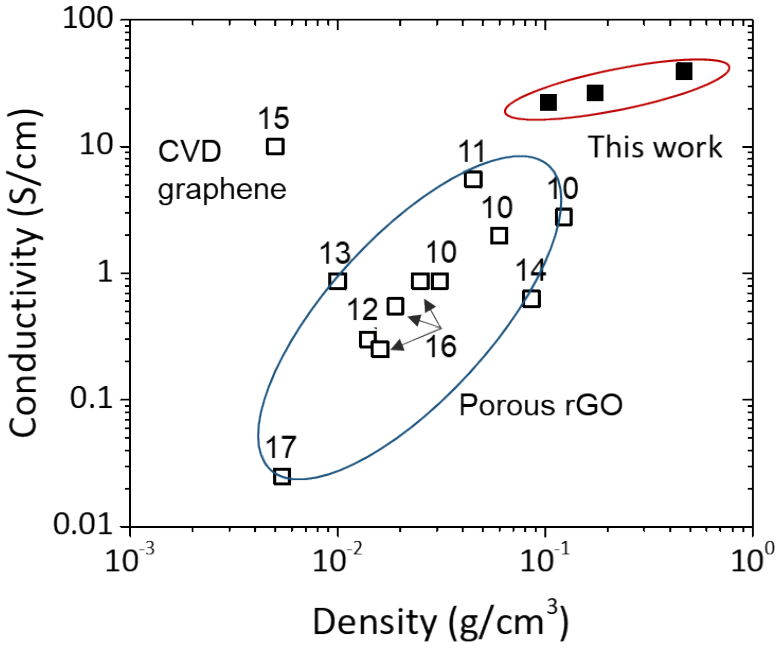


Figure S2. Electric conductivity of RGO carbonized from different NMP:TMPTA ratios (from left to right: 90/10, 70/30, 0/100) as the function of density and comparison with previous work.[10–17]

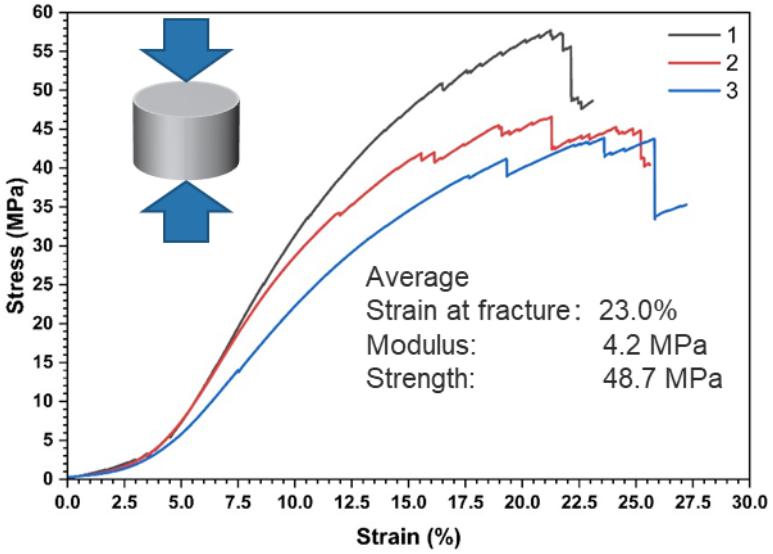


Figure S3. Compression strain-stress curves of 3D printed porous electrode samples with an NMP:TMPTA ratios of 90/10.

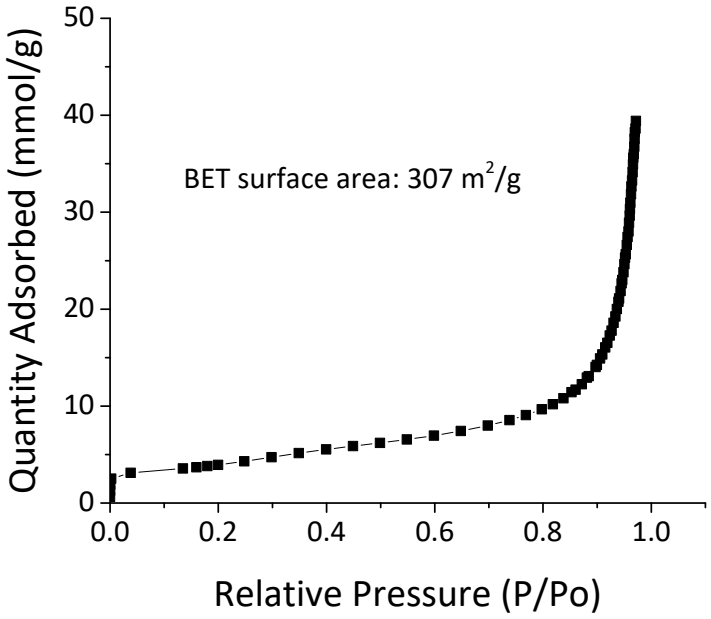


Figure S4. Adsorption branch of the $N_2$ sorption isotherm of the RGO derived from 4wt% GO in NMP/TMPTA (90/10) resin.

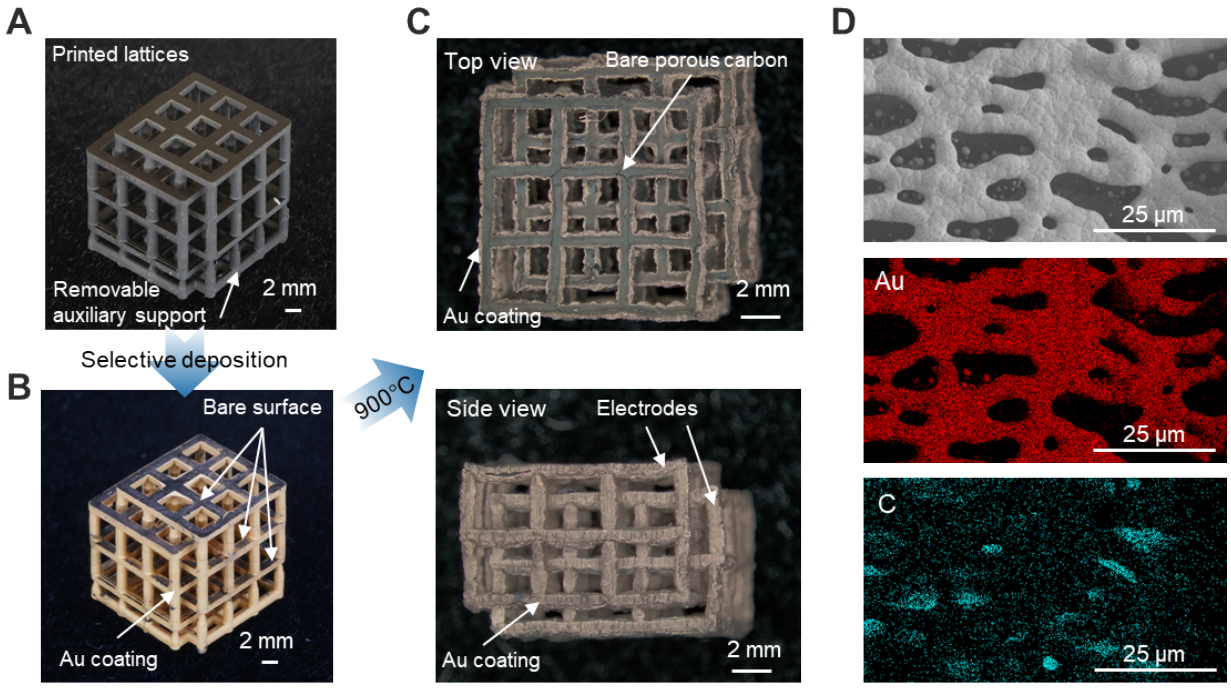


Figure S5. (A-C) Process of selectrive deposition. (D) SEM image and the elemental mapping of Au and C of the porous gold coating on the porous carbon electrode.

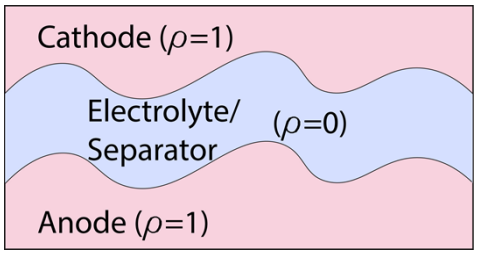


Figure S6. Two-dimensional design space of a full cell

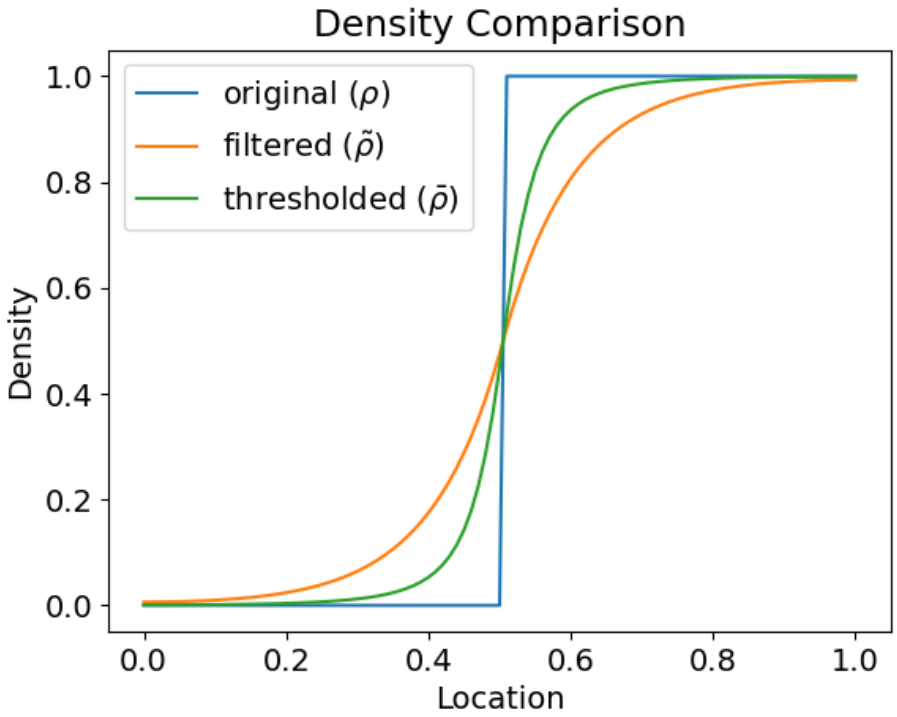


Figure S7. Comparison between original, filtered, and thresholded densities.

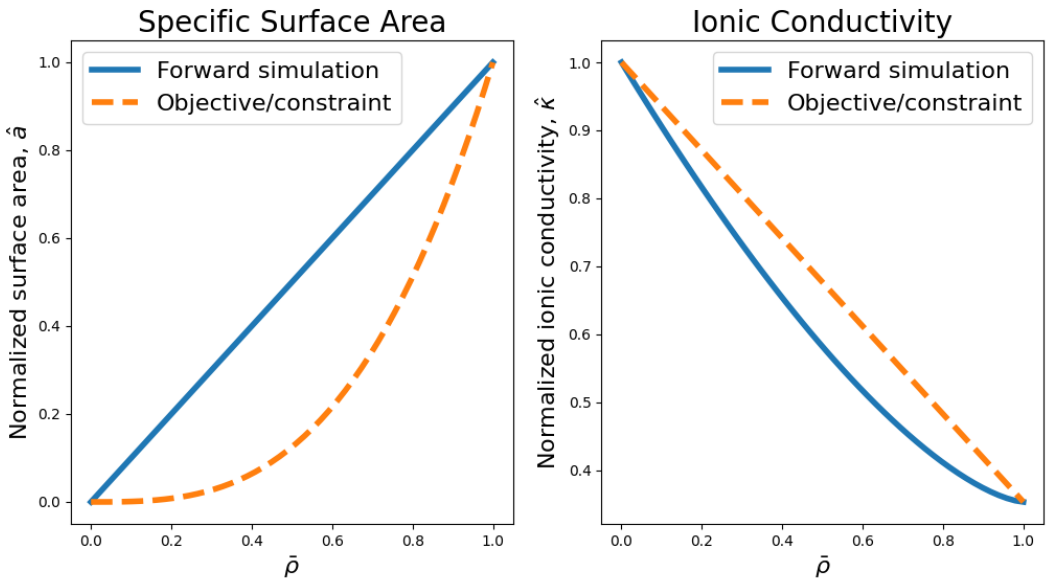


Figure S8. Comparison between parameter interpolations of forward simulation and QoI computations

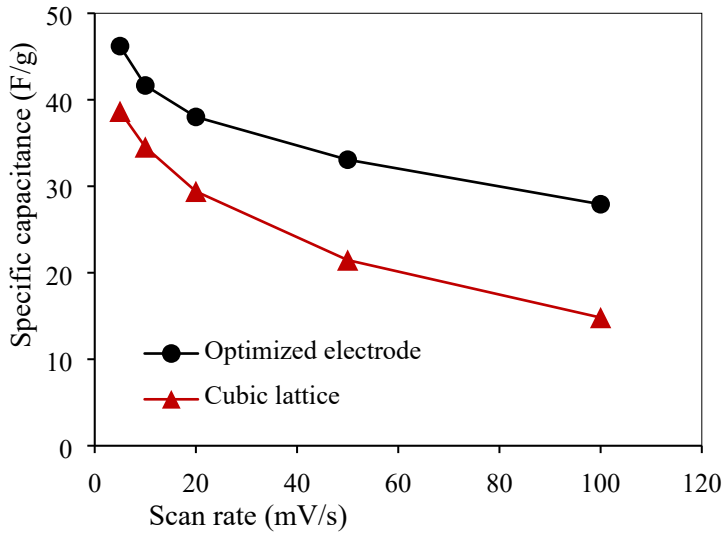


Figure S9. Rate capability of the electrodes with different structures at various scan rates.

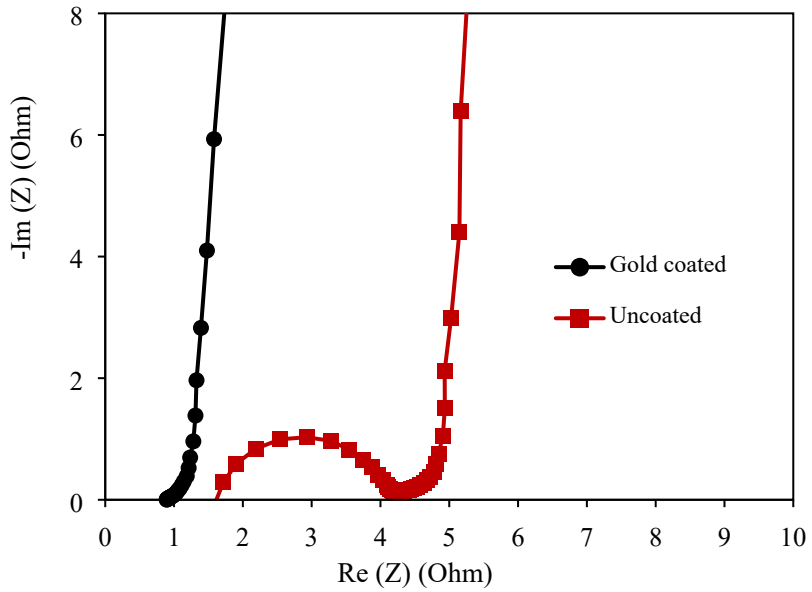


Figure S10. EIS of the structure optimized electrodes with and without gold coating.

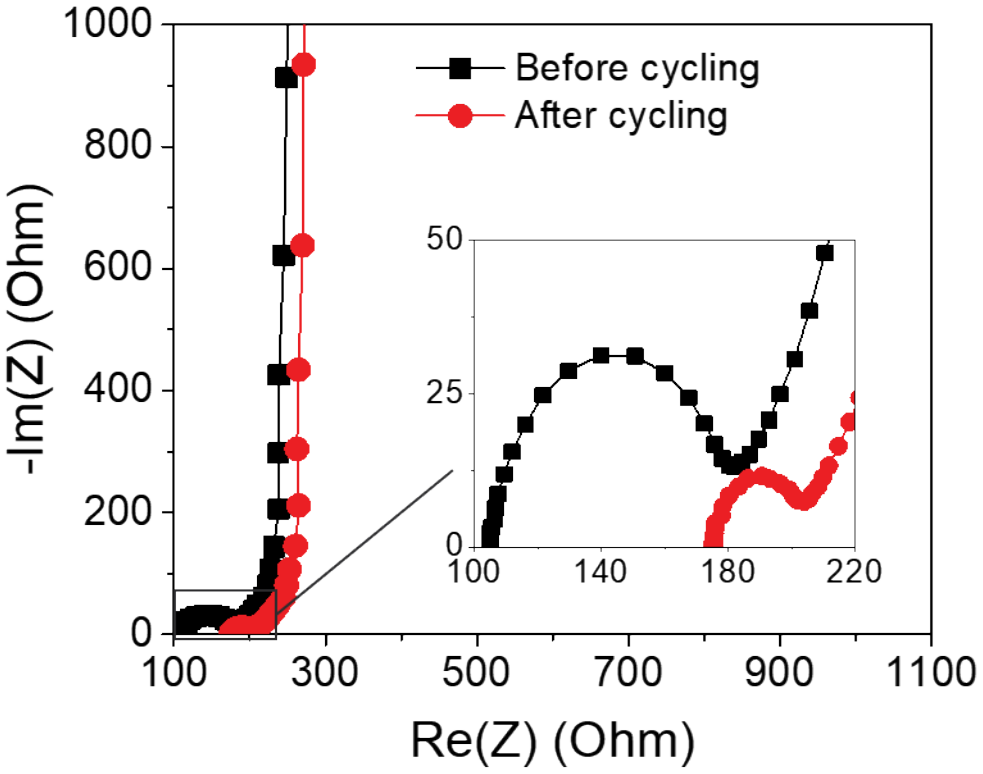


Figure S11. Nyqvist plots before and after the 7500 cycles of charge/discharge.

## References


(1) Newman, J.; Tiedemann, W. Porous-Electrode Theory with Battery Applications. *AIChE Journal* **1975**, *21* (1), 25–41. https://doi.org/10.1002/aic.690210103.

(2) Xu, Y.; Lin, Z.; Zhong, X.; Huang, X.; Weiss, N. O.; Huang, Y.; Duan, X. Holey Graphene Frameworks for Highly Efficient Capacitive Energy Storage. *Nat Commun* **2014**, *5* (1), 4554. https://doi.org/10.1038/ncomms5554.

(3) Li, H.; Bucci, G.; Brady, N. W.; Cross, N. R.; Ehlinger, V. M.; Lin, T. Y.; Salazar de Troya, M.; Tortorelli, D.; Worsley, M. A.; Roy, T. Topology Optimization for the Full-Cell Design of Porous Electrodes in Electrochemical Energy Storage Devices. *Struct Multidisc Optim* **2024**, *67* (11), 188. https://doi.org/10.1007/s00158-024-03901-z.

(4) Ham, D. A.; Kelly, P. H.; Mitchell, L.; Cotter, C.; Kirby, R. C.; Sagiyama, K.; Bouziani, N.; Vorderwuelbecke, S.; Gregory, T.; Betteridge, J.; Shapero, D. R.; Nixon-Hill, R.; Ward, C.; Farrell, P. E.; Brubeck, P. D.; Marsden, I.; Gibson, T. H.; Homolya, M.; Sun, T.; McRae, A. T. Firedrake User Manual. **2023**. https://doi.org/10.25561/104839.

(5) Mitusch, S. K.; Funke, S. W.; Dokken, J. S. Dolfin-Adjoint 2018.1: Automated Adjoints for FEniCS and Firedrake. *Journal of Open Source Software* **2019**, *4* (38), 1292. https://doi.org/10.21105/joss.01292.

(6) Svanberg, K. The Method of Moving Asymptotes—a New Method for Structural Optimization. *International Journal for Numerical Methods in Engineering* **1987**, *24* (2), 359–373. https://doi.org/10.1002/nme.1620240207.

(7) Troya, M. S. de. LLNL/pyMMAopt: Method of Moving Asymptotes for Firedrake, 2021. https://doi.org/10.5281/zenodo.4456055.

(8) Lazarov, B. S.; Sigmund, O. Filters in Topology Optimization Based on Helmholtz-Type Differential Equations. *International Journal for Numerical Methods in Engineering* **2011**, *86* (6), 765–781. https://doi.org/10.1002/nme.3072.

(9) Madabattula, G.; Kumar, S. Model and Measurement Based Insights into Double Layer Capacitors: Voltage-Dependent Capacitance and Low Ionic Conductivity in Pores. *J. Electrochem. Soc.* **2020**, *167* (8), 080535. https://doi.org/10.1149/1945-7111/ab90aa.

(10) Zhu, C.; Han, T. Y.-J.; Duoss, E. B.; Golobic, A. M.; Kuntz, J. D.; Spadaccini, C. M.; Worsley, M. A. Highly Compressible 3D Periodic Graphene Aerogel Microlattices. *Nat Commun* **2015**, *6* (1), 6962. https://doi.org/10.1038/ncomms7962.

(11) Worsley, M. A.; Pham, T. T.; Yan, A.; Shin, S. J.; Lee, J. R. I.; Bagge-Hansen, M.; Mickelson, W.; Zettl, A. Synthesis and Characterization of Highly Crystalline Graphene Aerogels. *ACS Nano* **2014**, *8* (10), 11013–11022. https://doi.org/10.1021/nn505335u.

(12) Kim, K. H.; Oh, Y.; Islam, M. F. Graphene Coating Makes Carbon Nanotube Aerogels Superelastic and Resistant to Fatigue. *Nature Nanotech* **2012**, *7* (9), 562–566. https://doi.org/10.1038/nnano.2012.118.

(13) Worsley, M. A.; Pauzauskie, P. J.; Olson, T. Y.; Biener, J.; Satcher, J. H. Jr.; Baumann, T. F. Synthesis of Graphene Aerogel with High Electrical Conductivity. *J. Am. Chem. Soc.* **2010**, *132* (40), 14067–14069. https://doi.org/10.1021/ja1072299.

(14) Xu, Y.; Sheng, K.; Li, C.; Shi, G. Self-Assembled Graphene Hydrogel via a One-Step Hydrothermal Process. *ACS Nano* **2010**, *4* (7), 4324–4330. https://doi.org/10.1021/nn101187z.

(15) Chen, Z.; Ren, W.; Gao, L.; Liu, B.; Pei, S.; Cheng, H.-M. Three-Dimensional Flexible and Conductive Interconnected Graphene Networks Grown by Chemical Vapour Deposition. *Nature Mater* **2011**, *10* (6), 424–428. https://doi.org/10.1038/nmat3001.
(16) Worsley, M. A.; Olson, T. Y.; Lee, J. R. I.; Willey, T. M.; Nielsen, M. H.; Roberts, S. K.; Pauzauskie, P. J.; Biener, J.; Satcher, J. H. Jr.; Baumann, T. F. High Surface Area, Sp2-Cross-Linked Three-Dimensional Graphene Monoliths. *J. Phys. Chem. Lett.* **2011**, *2* (8), 921–925. https://doi.org/10.1021/jz200223x.
(17) Hu, H.; Zhao, Z.; Wan, W.; Gogotsi, Y.; Qiu, J. Ultralight and Highly Compressible Graphene Aerogels. *Advanced Materials* **2013**, *25* (15), 2219–2223. https://doi.org/10.1002/adma.201204530.